D-shaped body wake control through flexible filaments

J. C. Muñoz-Hervás,[1,2] B. Semin,[3] M. Lorite-Díez,[2,4,*] G. J. Michon,[5]
Juan D'Adamo,[6,7] J.I. Jiménez-González,[1,2] and R. Godoy-Diana[3]

[1] *Departamento de Ingeniería Mecánica y Minera, Universidad de Jaén, Jaén, Spain*
[2] *Andalusian Institute for Earth System Research, Universities of Granada, Jaén y Córdoba, Spain.*
[3] *Laboratoire PMMH, ESPCI, CNRS, Sorbonne Université, Université Paris Cité. Paris, France.*
[4] *Departamento de Mecánica de Estructuras e Ingeniería Hidráulica, Universidad de Granada, Spain.*
[5] *Institut Jean Le Rond d'Alembert, CNRS, Sorbonne Université, UMR 7190, F-75005 Paris, France*
[6] *Facultad de Ingeniería Universidad de Buenos Aires, CONICET. Buenos Aires, Argentina.*
[7] *Institut Franco-Argentin de Dynamique des Fluides pour l'Environnement, IRL2027, CNRS, Universidad de Buenos Aires, CONICET. Buenos Aires, Argentina.*

(Dated: October 14, 2025)

In this study, we investigate the flow around a canonical blunt body, specifically a D-shaped body of width D, in a closed water channel. Our goal is to explore near-wake flow modifications when a series of rigid and flexible plates ($l = 1.8D$) divided into filaments ($h = 0.2D$) are added. We focus on assessing the interaction between the flexible filaments and the wake dynamics, with the aim of reducing the recirculation bubble and decreasing the velocity deficit in the wake. To achieve this, we conduct a comparative study varying the stiffness and position of the filaments at different flow velocities. The study combines Particle Image Velocimetry (PIV) measurements in the wake behind the body with recordings of the deformation of the flexible filaments. Our observations show that the flexible filaments can passively reconfigure in a two-dimensional fashion, with a mean tip deflection angle that increases with the incoming flow velocity. Deflection angles up to approximately $\sim 9^\circ$ and vibration tip amplitude of around $\sim 4^\circ$ are achieved for flow velocities $U^* \simeq u_\infty / f_n D \geq 1.77$, where f_n is the natural frequency of the flexible filaments. This reconfiguration results in a reduction of the recirculation bubble and a decrease in the velocity deficit in the wake and the estimated drag compared to the reference and rigid cases. In addition, curved filaments with a prescribed rigid deformation exhibit very similar behavior to that of flexible filaments, indicating that the vibration of flexible filaments does not significantly disturb the wake. The obtained results highlight the interest of testing flexible appendages in the wake of blunt bodies for designing effective flow control devices.

I. INTRODUCTION

The study of the flow around two-dimensional blunt bodies is a significant research field, as this configuration is common in many engineering and environmental applications, including civil structures such as bridges and buildings, as well as offshore structures like deep-water risers. In particular, flow separation at the rear of these bodies can generate vortex shedding, caused by Bénard-von Karman instability (BvK), leading to the formation of a low-pressure region. Research in this area is typically driven by practical goals such as reducing drag on the blunt body [1], suppressing flow-induced vibrations (FIVs) [2–4], or modifying heat transfer around a body immersed in a given flow [5].

In the study of two-dimensional bluff bodies, D-shaped geometries have been extensively analyzed, particularly due to their characteristic fixed separation point at the trailing edge [6–8]. For these geometries, the mean base pressure coefficient remains nearly constant along the third direction, with values around -0.6. This constancy emphasizes the wake's significant impact on overall drag, which ranges between 0.8 and 1 for the tested Reynolds numbers. The Reynolds number, defined as $Re = u_\infty D/\nu$, depends on the free-stream velocity (u_∞) the body diameter (D) and the fluid's kinematic viscosity (ν). In this configuration, vortex shedding occurs at a specific frequency, f, or equivalently, at a fixed Strouhal number $St = fD/u_\infty$, as for instance, $St = 0.25$ at $Re = 40.000$. The shedding process produces strong velocity fluctuations in the wake downstream of the body [7] that impact the body aerodynamics.

Various devices and strategies aim to actively or passively control the wake behind blunt bodies to reduce the averaged or fluctuating drag or lift force coefficients. Active control devices include pulsed jets [9, 10], plasma actuators [11], or suction/blowing strategies [12, 13]. Examples of closed-loop flow control include sinusoidal zero-net-flux actuation through spanwise slots [8, 14] and actuated flaps in 3D wakes [15]. However, implementing active

* mldiez@ugr.es

flow control systems in real-world applications often requires significant power input or sophisticated systems, limiting their practicality and efficiency. This makes passive control systems more attractive due to their simplicity.

Among passive strategies, initial studies by [16] examined the effect of including plates at the body base, while other more recent studies introduced trailing edge modifications such as small tabs [7], base cavities [17–19] and boat-tailed after-bodies [20–22]. Rear cavity devices can be further refined with multi-cavity arrangements [23] or optimized geometries focused on reducing drag [24]. The efficiency of rear cavities in terms of drag reduction is linked to their depth, as they move the wake formation away from the body base, generating a dead flow region that effectively increases base pressure.

However, their aerodynamic efficiency may be reduced under different flow conditions, such as accelerated flows from rest [25] or yawed orientations [26]. An interesting approach that can adapt to different flow conditions involves using bio-inspired flexible devices, modifying the rear part of the body into a more aerodynamic shape through passive reconfiguration [27–29]. This process is commonly observed in nature, where the reconfiguration of flexible parts [30, 31], such as leaves in trees, reduces aerodynamic resistance and effective area [32] under different wind conditions, (see [33], for a review). The passive reconfiguration of flexible systems to modify the wake behind bluff bodies has been only scarcely investigated [34]. Recent studies [28, 29] propose using rotary and flexible flaps to configure a self-adaptive cavity, achieving drag reductions of up to 18% by reducing the wake bluffness and streamlining rear separation.

Despite these advantages, the practical implementation of these devices may face challenges, such as ensuring uniform mechanical properties in movable parts with large length-to-thickness ratios and managing significant loads and potential torsional deformations. As an alternative, we propose using a modular system based on an array of small filaments that can function as a single flexible flap with much lower mechanical loads. In the case of rigid arrays of filaments, [35] examined the use of porous rear cavities in 3D blunt bodies, finding similar results for modular cavities with small spacing between elements and fully solid rear cavities. Additionally, the device studied here incorporates the degrees of freedom associated with the flexibility of the filaments, allowing the elements to adapt their shape to the eventual three-dimensional features of the flow around the D-shaped body.

In this work, we aim to study the effect of modular arrays of filaments resembling a cavity to manipulate and control the wake behind a D-shaped body. The tested devices comprise an array of flexible filaments that interact with the incoming flow, adapting their shape to different conditions. We will experimentally assess the interaction between the filaments and the wake by measuring filament motion and wake features. The experimental details are presented in Sect. II, followed by the main results in Sect.III. There, Sect. III A describes the flexible filaments motion, Sect. III B covers the temporal synchronization between filaments and vortex shedding, and Sect. III C presents the wake features for the four tested configurations. The main conclusions are drawn in Sect. IV.

II. EXPERIMENTAL SETUP

The experiments were carried out in a closed water channel with a cross section of 0.1×0.1 m^2 and a turbulence intensity below 3%, whose test section, shown in Fig. 1a, must be emptied to introduce any modification in the experimental setup. This water channel has been characterized and used in previous studies focused on 3D bluff body wakes as [36–38]. Here, the D-shaped body used has a characteristic diameter D of 20 mm, a length $L = 3.6D$ and height $H = 5D$, which matches the height of the test section. By spanning the height of the body along the channel's height and minimizing the gap between walls and body sides, we try to avoid the three-dimensional effects stemming from the body-edges. The blockage effect and the development of boundary layers in the channel walls have been taken into account in our study, appropriately re-scaling the results for all flow conditions tested as in [39]. In this case, the mean incoming velocity is first obtained using the measured flow rate. Then, a scaling factor based on PIV measurements has been considered for areas of the measurement area not affected by blockage, boundary layer development, or the body, where the velocity should be equal to u_∞. The scaling factor is almost 1.5 for the smallest incoming velocity and close to one for the largest incoming velocity.

In our experiment, the coordinate system is centered at the body base, with the x-axis aligned with the streamwise direction, the z-axis pointing vertically, and the y-axis completing a right-hand trihedron. In that reference frame, the rotations in the anti-clockwise direction are considered positive. Four different configurations are tested and compared, including the reference body with blunt trailing edges (reference), and three configurations that contain two arrays of filaments with different stiffness and shapes implemented in the trailing edges of the D-shaped body. Each array contains 17 filaments, with length $l = 1.8D$ and height $h = 0.2D$. Each filament is separated from the following one by $d = 0.1D$ so the filaments are free to move separately, while presenting a semi continuous flap as in [35]. The filaments are made of TPU (Thermoplastic Polyurethane) 92A with an elastic modulus of $E_F = 16$ MPa (Flexible) and made of PLA (polylactic acid) with $E_R = 3600$ MPa (Rigid). In the case of rigid arrays of filaments, we have tested two shapes of filaments, one aligned with the body trailing edges (straight) and one with a given curved

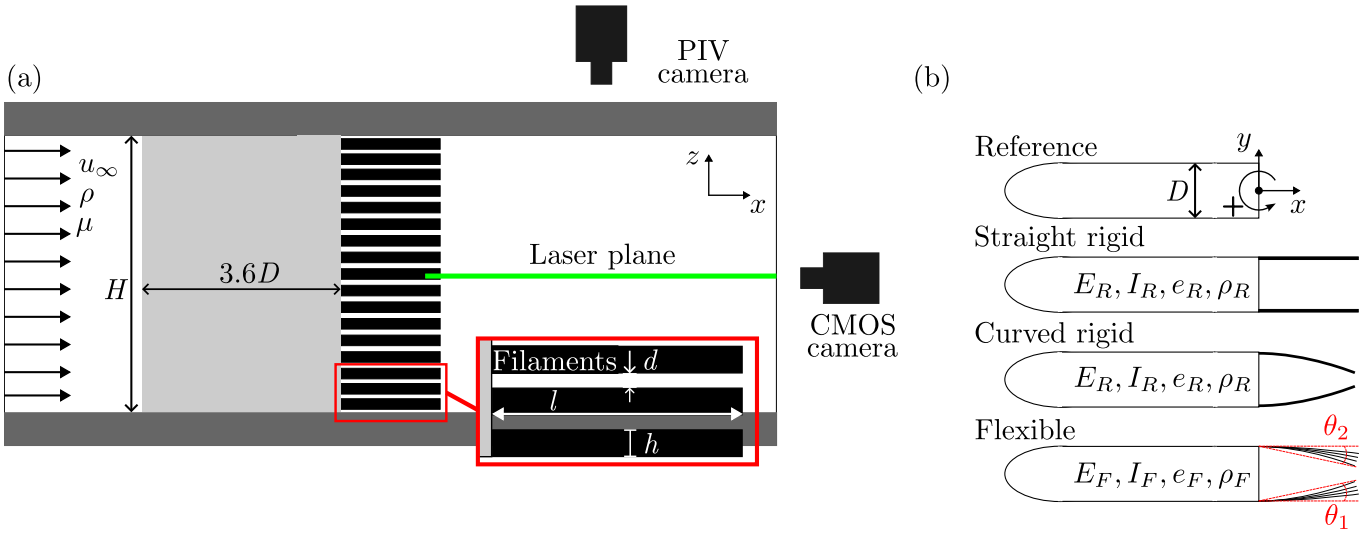

Figure 1. (a) Sketch of the experimental set-up and (b) Tested rear configurations and their corresponding characteristic parameters.

deformation (curved), corresponding to a tip deflection angle of 11° for a first Euler-Bernoulli vibration mode. This reconfiguration angle is the maximum reconfiguration observed for a single flexible filament in our experiment. The height of the body has been adjusted to mimic that of the water tunnel, but a distance of 1 mm has been set between the filaments and the walls to allow them to move freely. However, due to the formation of boundary layers inherent to any water tunnel experiment, the local flow velocity in the upper and lower filaments is affected by the proximity of the walls, thus modifying their response, as we will later discuss.

The arrays of filaments were first designed through CAD and then manufactured using 3D printers. In particular, the flexible filaments were produced with an Artillery X2 printer using TPU (Thermoplastic polyurethane), specifically TPU-92A from Kimya. The number 92A refers to the hardness in shore scale, the reported young modulus (16 MPa) from the vendor does not differ from our measurements. For the rigid filaments, a printer Stratasys Fortus 250mc was employed using PLA. In addition to changing the employed material, different filament thicknesses were used to manufacture appropriate rigid (not interacting with flow) and flexible filaments. For the flexible ones, a thickness, $e_F = 0.01D$ is used, while for the straight and curved ones, thickness, $e_R = 0.05D$ is employed. Regarding the flexible filaments, the dimensions were meticulously selected to induce a desired response within the range of flow velocities of the experiments. To that aim, arrays of filaments of different lengths and thicknesses were designed and tested to achieve a sufficient reconfiguration capacity.

it is necessary to couple the characteristics of the device with the range of flow velocities in the channel. In particular, the flexible filaments must reconfigure before the maximum flow velocity is reached. To meet this requirement, arrays of filaments of different lengths and thicknesses - key flexibility parameters - were designed and tested. If the material/thickness made the filament too stiff, it wouldn't deform enough with flow. If the filament was too long, it could touch the filament on the other array. The preliminary tests helped us to refine the design and the final parameters presented in the paper.

The employed water channel works in a range of free-stream velocities ranging between 0.05 and 0.28 m/s, corresponding with Reynolds numbers from 1060 to 5200. Accordingly, the reduced velocity, defined as the ratio between the free-stream velocity and the averaged velocity of the flexible filaments movement, $U^* = u_\infty / f_n D$ results within the interval $[0.5, 2.45]$. The velocity of the filaments is determined by the flexible filaments corresponding natural frequency. This natural frequency in vacuum has been firstly obtained with the following equation:

$$f_n = \frac{\beta^2}{2\pi}\sqrt{\frac{EI}{\rho_F e_F h l^4}}, \tag{1}$$

where β is a coefficient given by the Euler-Bernoulli deflection mode for a cantilevered beam, I the moment of inertia of one filament around the bending axis and ρ_F the density of the TPU 92A, which is the material employed for the flexible filament array. The obtained result ($f_n = 5.7\ Hz$) matched accurately the natural frequency measured in free-decay tests ($f_n = 5.67\ Hz$) made in air. These tests were conducted using a position laser sensor and initially displacing the filaments from their equilibrium position. Note that no valid free-decay tests are available for plates

in water, as the motion is quickly damped; nevertheless, a simplified theoretical estimation of the natural frequency in water, following [29], provides a value of $f_{n,w} \leq f_n/3$. This approximation does not consider any added mass coefficient and therefore, its use for a deeper analysis of results has been discarded.

We carried out PIV measurements on the 4 employed configurations to analyze the wake behind the D-shaped body in the xy plane for each case. To generate the illuminated measurement plane, we horizontally positioned at $z = 0$ a laser sheet generated by a Quantel Big Sky double pulsed Nd:YAG laser with 532nm emision with 250mJ per pulse at 10 Hz, as shown in Fig.1 (a). That laser illuminated polyamide particles with a characteristic diameter of 20 μm (Lavision HQ polyamide beads). To capture the seeding particle images, we employed a PIV system comprising a LaVision® PTU-X synchronizer and a SCMOS Imager Pro Plus 2M 12-bits camera equipped with a Nikon 50mm objective and an aperture fixed at f/5.6 (see PIV Camera in Fig.1). The resulting images were 1600 × 1200 pixels and were calibrated by measuring the distance between the channel walls, yielding a magnification factor of 10.58 px/mm. The recordings were conducted at a frequency of 10 Hz with laser pulses delayed by approximately 0.7 to 3 ms, capturing a total duration of 60 s (600 pairs of images per experiment). After correctly setting the region of interest (123 × 87 mm), velocity vectors were obtained from cross-correlation in Davis 10 from LaVision® with interrogation windows of 32 × 32 pixels with an overlap of 50%, resulting in a spatial grid of 83 × 59 points. The PIV measurement plane was set to cover the largest possible wake region, $x/D \in [0, 6], y/D \in [-2, 2]$ for the reference case, while maintaining a reasonable resolution (13 vectors in the body diameter, D) so that we could characterise the near and far wake and avoid laser reflections on the filaments. Finally, our measurements have a correlation-based uncertainty [40] typically below 3% of the free-stream velocity for both u_x and u_y.

In addition, for the flexible filaments, after characterizing their mechanical properties, we recorded their tip deflection with a Basler ACE acA2000-165um CMOS camera, equipped with a CMV2000 Sensor, which is capable of acquiring 2048 × 2048 pixel images at a maximum frame rate of 165 fps. Thanks to the available optical access at one end of the water channel, this camera was able to characterize the filaments motion in the zy plane. In order to track this motion, each filament edge was highlighted with white dots which were illuminated by a high-power LED lamp. The camera recordings were made at 134 fps and the exposure time was adjusted to capture static white dots. To analyze the captured images, we employed the open-source image processing tool DLTdv8 [41], which can be integrated as a toolbox within Matlab®. This tool allows precise tracking of specific points in a video. Initially, it conducts an image analysis based on a predetermined threshold, followed by contour detection facilitated by intensity discrepancies.

In terms of the experimental measurements reliability and precision, we repeated the deformation and PIV measurements for two specific Re numbers (1196 and 3635) without observing any significant differences between analogous tests at the same experimental conditions. This approach enabled the calculation of error estimates for these Re, yielding an error below 5% (represented by error bars in Fig. 3).

In the following, time-dependent variables will be denoted using lower-case letters a, while time-averaged values will be expressed with upper-case letters $A = \overline{a}$. In addition, $\hat{a}$ will denote the instantaneous fluctuating amplitude of the variable a, which will be computed by means of the Hilbert transform, so that $\hat{A}$ will represent the corresponding time-averaged fluctuating amplitude. On the other hand, the notation $\mid A \mid$ will be used to indicate the modulus of a variable. Finally, $\langle a \rangle$ stands for the spatial average of a variable.

III. RESULTS

A. Response of the flexible filament array

We will firstly analyze the motion of the two arrays of filaments. The tip deflection of the 34 flexible filaments (17 on each side) is captured by a rear view that allows to compute the tip angles, θ, by using trigonometric transformations and the filament length, l. The reference position for the lateral displacement is the reference body trailing edge. We also checked that the filaments were deformed according to a first Euler-Bernoulli deflection mode for a cantilevered beam by supplementary recordings from the top of the water channel (the recording location is similar to the one of the PIV camera). The analysis of the captured images depicts that all filaments bend on average inward the wake while describing a periodic fashion once a certain flow velocity is set. They move in phase along the span as well as between the two arrays of filaments. The analysis of the temporal deformation of the filaments provides both the mean deflection angle Θ and the angular oscillation amplitude $\hat{\Theta}$ for each filament, whose spanwise distributions for $U^* \simeq 1.77$ ($Re \simeq 3636$) are shown in Fig. 2. The filaments on the left ($y < 0$), θ_1, and right ($y > 0$), θ_2, sides are shown along the spanwise direction, z. Figure 2 (a) shows a clear reaction in a quasi-static 2D way of the flexible filament arrays under the influence of the flow. At the depicted U^*, the flexible filaments reach an averaged tip deflection around 9° along with moderate oscillations of approximately 4° (see Fig. 2b). The spanwise distribution of the flexible filaments deflections and oscillations shows a seemingly constant behaviour in the central part of the

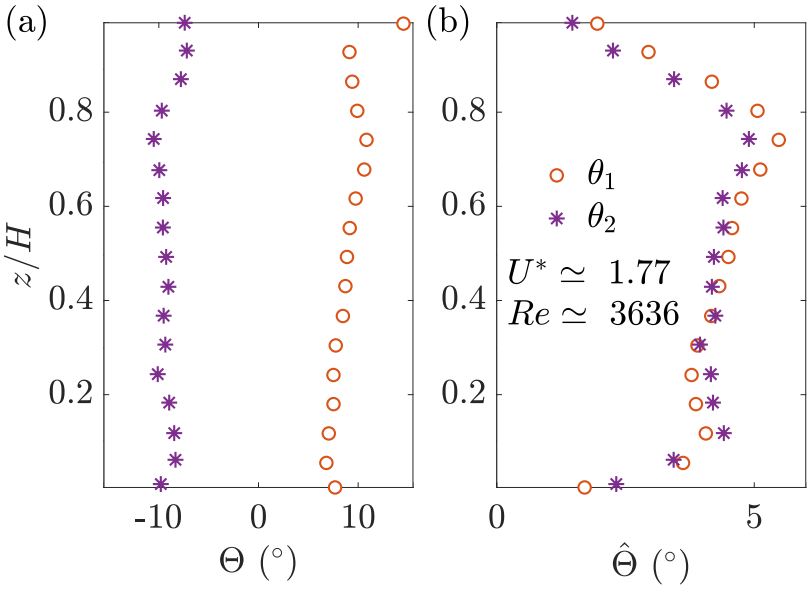

Figure 2. (a, b) Time-averaged tip angle deflection, Θ, and the corresponding averaged oscillations amplitude, $\hat{\Theta}$, for the flexible filaments along the spanwise direction, of the D-shaped body at $Re \simeq 3636$ and $U^* \simeq 1.77$. We depict in orange circles the filaments on the left side ($y < 0,\ \theta_1$) and in purple asterisks those on the right side ($y > 0,\ \theta_2$).

D-shaped body with distinguishable differences close to the water channel walls ($z/H < 0.15$, $z/H > 0.85$). There, the response of filaments placed close to walls is likely to be affected by velocity gradients defining the boundary layers and 3D edge structures, which cannot be avoided in the closed water channel set-up the local velocity. However, for the sake of simplicity, the approximately uniform response in the central part, will be used, in a first approximation, as an estimation of the quasi two-dimensional response of the arrays of filaments.

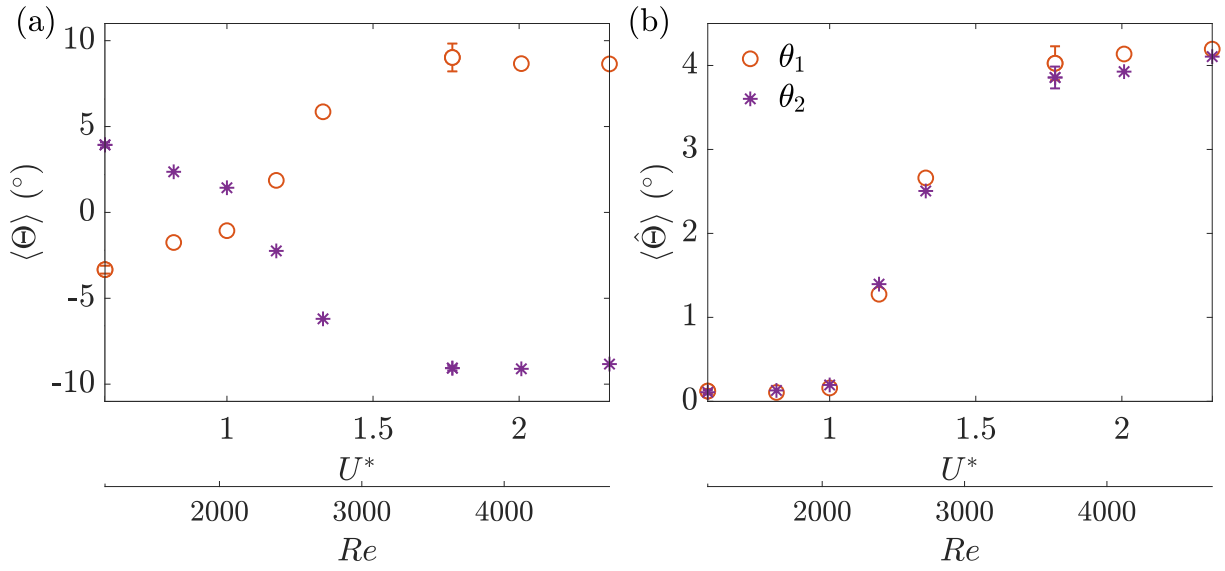

Figure 3. Evolution of (a) the spatio-temporal averaged tip deflection angle, $\langle\Theta\rangle$, and (b) the spatio-temporal averaged amplitude of tip angle oscillations, $\langle\hat{\Theta}\rangle$, with respect to U^* and Re. We depict in orange circles the filaments on the left side ($y < 0,\ \theta_1$), and in purple asterisks those on the right side ($y > 0,\ \theta_2$). Error bars depicted for selected values of U^* quantify the standard deviation of the measurements for repeated experiments.

The evolution of the mean tip deflection angle, averaged in time and in space across the spanwise direction, is presented in Fig. 3 (a) for the range of U^* (Re) tested here. The mean deflection, $\langle\Theta\rangle$, increases with increasing Reynolds numbers and reduced velocities until reaching a saturation value, around 9°, at $U^* \simeq 1.77$ or $Re \simeq 3636$.

This absolute increase of the deflection shown by $\langle\Theta\rangle$, has an opposite sign for each array of filaments, due to the sign convention employed, where a rotating angle in the counterclockwise direction is positive (see Fig. 1b). Thus, the filaments on the left side (θ_1) have increasingly positive angles as filaments deflection increases with U^* whereas the ones on the right side (θ_2), depict increasingly negative angles with increasing U^*. Furthermore, it is noteworthy that there is an initial part of the range, until $U^* < 1$ and $Re < 2052$, where an initial deformation in the outward direction is observed for both flaps, meaning that the position of the filament tips extends beyond the limits of the D-shaped body. This is why both data series cross $\langle\Theta\rangle = 0$ immediately after $U^* \simeq 1$ ($Re \simeq 2052$). In absolute terms, this region with a negative mean deflection indicates that the flow momentum is insufficient to deform and move the filaments and the filaments preserve their initial random dry loading. The evolution of the mean tip deflection angle depicted in Fig. 3 (a) illustrates an increasing passive reconfiguration of the flexible filaments in the studied range of U^* (Re) for both arrays of flexible filaments for reduced velocities above $U^* > 1$, what may lead to efficient reduction of the drag coefficient. However, the passive reconfiguration reaches a saturated state around $\Theta = 9°$ for $U^* > 1.77$, suggesting a limit on the potential for drag reduction from this point onward, that may translate into an asymptotic value of the Vogel exponent [see e.g. 42] (note that such a negative exponent is typically used to quantify the aerodynamic effect of passive reconfiguration of flexible structures [29, 32]).

Regarding the filaments vibrations, the spatio-temporal averaged amplitude of the tip angle fluctuations, $\langle\hat{\Theta}\rangle$, is shown in Fig. 3 (b). Again, both arrays of flexible filaments show a very similar behaviour on both sides of the D-shaped body. The evolution of $\langle\hat{\Theta}\rangle$ depict a classical Stuart-Landau bifurcation behaviour with a critical reduced velocity close to $U^* \simeq 1$, matching the start of the passive reconfiguration observed for the average tip angle, $\langle\Theta\rangle$ in Fig. 3(a). Below this value, the filament oscillations are very low or practically non-existent ($\langle\hat{\Theta}\rangle < 0.2°$), confirming that the flow loading is unable to excite the flexible filaments at those velocities. Then, a sudden increase in the oscillations takes place reaching up to $\langle\hat{\Theta}\rangle \simeq 4°$ for $U^* = 1.77$ or $Re = 3636$, matching again the saturation phase of $\langle\Theta\rangle$ growth. The attained value can be considered as a saturation of the non-linear coupling between the wake flow and the flexible filaments, since further increasing of the flow velocity ($U^* > 1.77$) leads to a quasi-saturation zone of the filaments oscillations amplitude. We will analyze further this saturation phase in terms of temporal/frequency locking. However, it is worth mentioning that unlike the average angle, $\langle\Theta\rangle$, in which the saturated zone had a constant or even decreasing mean deflection, in the case of the filaments oscillations, there is a small increase in the vibration magnitude. For the maximum U^* and Re, the flexible filaments deflect with an averaged deformation around 8.6° along with a vibration of 4.2°, exhibiting a nearly symmetrical behavior on both sides of the body. Therefore, in the following, we will use the averaged data from both arrays of filaments. The performed experiments present a good reliability and precision, since the error bars included in Fig. 3 for $Re \simeq 1196, 3635$ correspond to very little dispersion.

B. Fluid-structure interaction

In this section, we discuss the connection between the flexible filaments and the vortex shedding behind the D-shaped body. The Power Spectral Density (PSD) related to the spatially averaged flexible filament motion, $\langle\Theta\rangle$, and the transverse flow velocity fluctuations, u'_y, are presented in Fig. 4 (a). These measurements were taken at the location of maximum transverse velocity fluctuations, specifically at $(4.25D, -0.4D, 0)$, for the flexible filament case, corresponding to $U^* \simeq 1.80$ ($Re \simeq 3800$). The wake information is derived from the temporal evolution signals captured through PIV measurements. At the selected flow conditions, the filaments are passively deflected and vibrating which causes the appearance of an energetic peak around $f^* = f/f_n \simeq 0.52$ ($St \simeq 0.28$), indicating a nearly periodic behaviour for the flexible filaments oscillation. In terms of vortex shedding, the velocity probe depicts a frequency peak close to the vibration frequency, which may indicate some synchronization between the flexible filaments and the shed vortices. As the filament deformation and wake velocity field are not recorded in the same experiment, experimental conditions may slightly differ, likely inducing the small differences in the identified dominant frequency.

To further analyze this temporal locking, Fig. 4(b) depicts the trend of the dominant frequencies obtained from the filaments motion, $\langle\Theta\rangle$, at the tested reduced velocities, U^* (Re) with black asterisks. Additionally, the vortex shedding dominant frequency is also represented with orange squares. This frequency is obtained from the fluctuating transversal velocity temporal evolution at (4.25D, -0.4D, 0). Finally, a Strouhal law, corresponding to the averaged dominant vortex shedding frequency of the D-shaped body ($St = 0.27$) is depicted in a green dashdotted line in Fig. 4(b) for the sake of comparison. Note that the associated values of Re (or St) are not exactly the same between PIV and visualization high-speed visualizations as they were recorded separately in successive experimental runs, as these two measurement methods cannot be performed simultaneously. The lack of synchronization between both experimental techniques results into slight differences in the value of the dominant frequencies (see fig. 4a), as the data were likely obtained at slightly different incoming velocities. The small uncertainty in f^* values has been computed

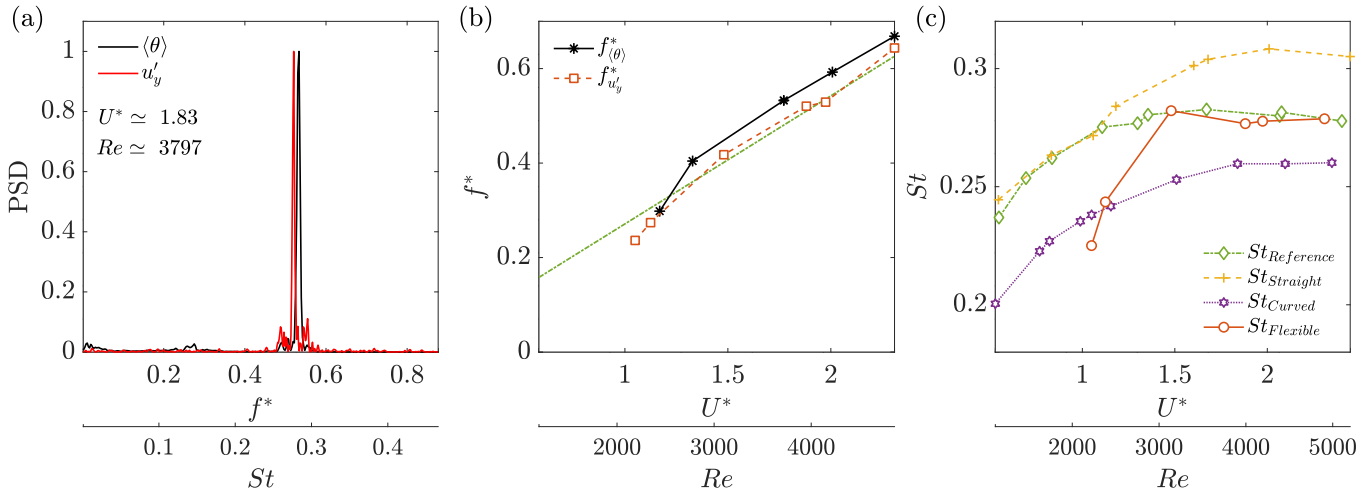

Figure 4. (a) PSD spectra of spatial averaged tip angle deflection signal and transverse velocity fluctuations located at (4.25D, -0.4D, 0) for $U^* \simeq 1.83$ ($Re \simeq 3797$). (b) Dominant frequencies of the filament tips' fluctuations ($f^*_{\langle\theta\rangle}$) in black solid asterisks. The vortex shedding dominant frequency ($f^*_{\langle u_y\rangle}$) for the flexible filaments is included in orange squares. A Strouhal law for the reference case ($St \simeq 0.27$, with $f^* = St \cdot U^*$) is also included with a green dashdotted line. (c) Strouhal, St, number evolution with U^* (Re) for vortex shedding in the reference case (green solid line and diamonds); straight rigid filaments (yellow dashed line and crosses); curved rigid filaments (purple dotted line and stars) and flexible filaments (orange solid line and circles) attached to the D-shaped body.

to yield an error of approximately $\Delta f^* \simeq 0.03$.

As observed in fig. 4(b), the amplitude response of filaments begins at $U^* = 1.13$ for which $f^*_{\langle\theta\rangle} \simeq 0.3$. This value might be close to the expected natural oscillation frequency of the filaments in water, $f_{n,w} \leq f_n/3$ [29], what promotes the beginning of oscillations. That said, since the exact value of $f_{n,w}$ is not known here, the data has been analyzed considering f_n). Results show that the dominant frequencies of vortex shedding, $f^*_{u'_y}$, and filaments oscillations, $f^*_{\langle\theta\rangle}$, are similar (slight differences are accountable to implicit errors from the different experimental techniques used) and increase linearly with U^*, following approximately the Strouhal law defined by the shedding frequency associated to the reference case. As shown in other flow-induced vibrations problems [see e.g. 29], the beginning of the amplitude response is typically guided by the Strouhal law during the initial branch, defined at low values of reduced velocities U^*. Thus, we presume that the oscillating dynamics reported here is exclusively characterized by an initial branch like response.

A complementary analysis focusing on the evolution with the reduced velocity of the vortex shedding frequency, given by the corresponding dimensionless Strouhal number $St(U^*)$, is included in Fig.4(c). As observed therein, all configurations show an initial increase of the Strouhal number, followed by a subsequent saturation phase, which is a typical feature of transitional regimes [43]. When flexible and curved filaments are employed, the vortex shedding frequency is generally reduced. Interestingly, the wake is almost steady for $U^* < 1$ ($Re < 2052$) when the flexible filaments are mounted, and therefore, no values are depicted for that trend of $St(U^*)$. This reduction of St displayed by filaments configurations seems to be related to the modification of the wake formation, as we will describe later.

To analyze the near wake changes induced by the reconfiguration of the flexible filaments, we next focus on a selected value of the reduced velocity $U^* \simeq 2.38$, corresponding to a Reynolds number of $Re \simeq 5015$. This reduced velocity displays the deformation of the flexible filaments that most closely resembles the shape of the curved rigid filaments, allowing for a meaningful comparison between both configurations. In this regard, Figure 5 illustrates phase-averaged snapshots of spanwise vorticity contours and velocity field flow vectors, for an equivalent shedding phase, for the different configurations. In particular, straight filaments seem to produce more elongated shear layers, producing smaller transversal velocities in the near wake in comparison with the other cases. In addition, the velocity vectors appear to be aligned with the incoming flow direction for the straight cavity configuration, indicating a nearly horizontal separation angle. On the other hand, the slanted shape of the curved and flexible cases induce an inward flow separation angle, evidenced by the vectors direction, that reduces the recirculation region bluffness as shown in Fig.5 (c,d) and increases the transverse velocity in the near wake. This decrease of the recirculation region bluffness has been shown to reduce both the drag and the shedding frequency in D-shaped bodies wakes [29]. The magnitude of the vortices in the wake is also reduced, although the flow disturbance extends further downstream. More importantly, these two configurations eliminate areas of negative streamwise velocity in the near wake.

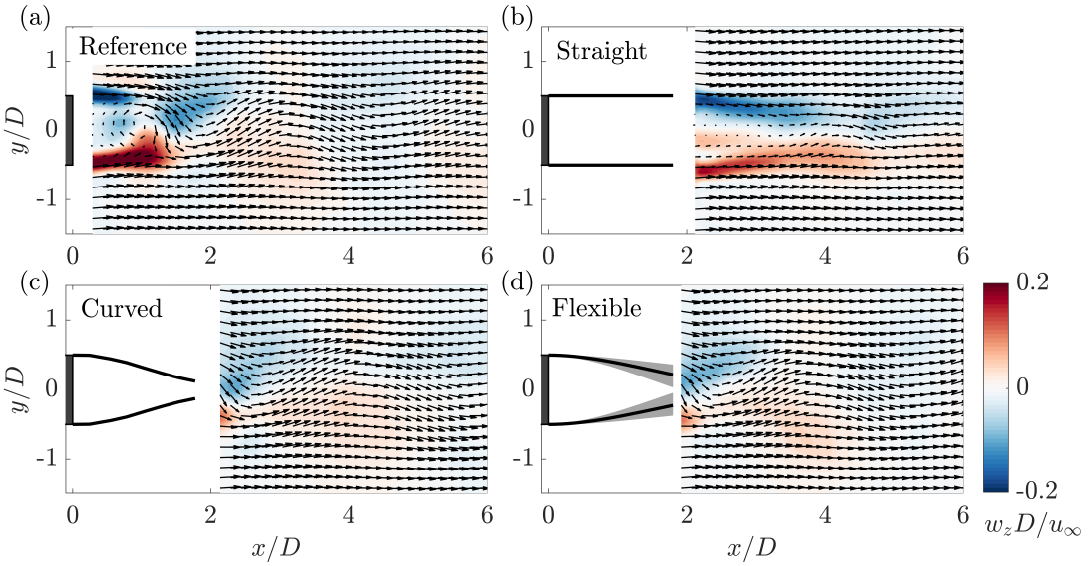

Figure 5. Contours of phase-averaged spanwise vorticity ($w_z D/u_\infty$) and the corresponding flow vectors (U_x, U_y) at $Re \simeq 5015$ ($U^* \simeq 2.38$). The four configurations are depicted: (a) Reference case; (b) Straight rigid filaments; (c) Curved rigid filaments and (d) Flexible filaments. In (d) the filament vibrations are represented by a gray area, while the spatio-temporal averaged filament deflection is shown in black. One over two vectors are represented for the flow field.

C. Effects of the different filament configurations on the near wake

Figure 6 depicts the time-averaged contours of the streamwise velocity, U_x, and the streamwise velocity fluctuations amplitude, $\hat{U}_x$, for the four tested configurations: Reference (a), Straight (b), Curved (c) and Flexible (d) cases. In addition, we depict the corresponding averaged flow streamlines (U_x, U_y). At $Re \simeq 5015$ ($U \simeq 2.38$), the flow around the reference D-shaped body produces a near wake composed by two symmetric recirculating zones, whose extension is up to $x \simeq 1.25$. The massive flow separation at the body trailing edges generates vortex shedding provoking important flow fluctuations in the near wake (see Fig. 6a). The extension of the recirculation region is considerably reduced when rigid straight flaps are mounted, also weakening the recirculating velocity magnitude. In addition, the presence of the flaps prevents the flow to recirculate close to the body base, but increases the area with small velocities, in accordance with the elongated vortices depicted in Fig. 5b). As a consequence, a dead-flow region is formed near the body base. The straight flaps are also able to reduce the unsteadiness in the near wake by reducing velocity fluctuations, as shown in Fig. 6(b). When the curved and flexible filaments are mounted, the wake features are pretty similar (see Fig. 6c,d). Both configurations are able to suppress the recirculation regions downstream of the flaps trailing edges. However, they both increase the flow fluctuations in comparison with the Straight case. These devices can deviate the flow at detachment, inducing an inward separation that generates additional flow fluctuations, as noted in [44, 45]. While these fluctuations may hinder drag reduction, the elimination of the recirculation region behind the body will ultimately lead to a significant reduction in drag, as we will see later. Additionally, flexible filaments introduce more unsteadiness in the wake than curved ones, particularly at velocities around $U \sim 2$. This increased excitation of the vortex shedding process may be linked to filament vibrations, illustrated by the gray areas in Fig. 6(d)

Additionally, to analyze the changes induced by the filaments on the near wake, we depict the velocity distributions downstream the D-shaped body for the different configurations using the averaged velocity profiles represented in Fig. 7. In particular, the axial and cross-sectional velocity profiles for streamwise and transversal velocities (averaged and fluctuations amplitude) are compared for the 4 tested configurations. Furthermore, the turbulent kinetic energy, computed as $k = 1/2((\hat{U}_x/u_\infty)^2 + (\hat{U}_y/u_\infty)^2)$, transversal profile is also included. The streamwise distribution of U_x at $y = 0$ (Fig. 7a) shows quantitatively the effect of the different rear geometries previously depicted in Fig. 6. In comparison with the reference case, the straight filaments attenuate the recirculation region and the velocity gradient outside the recirculation region at $Re \simeq 5015$ (see Fig. 7a). As shown in the same figure, both curved and flexible filaments are able to suppress the negative velocity values, decreasing the velocity deficit downstream the filaments trailing edges. The similarities between these configurations are based on the similar averaged orientation of the flexible filaments ($\langle\Theta\rangle \simeq 9°$) in comparison with the curved filaments (11°) at $U^* \simeq 2.31$. The performed comparison can also be made in terms of streamwise velocity fluctuations, which are mainly associated to vortex shedding in

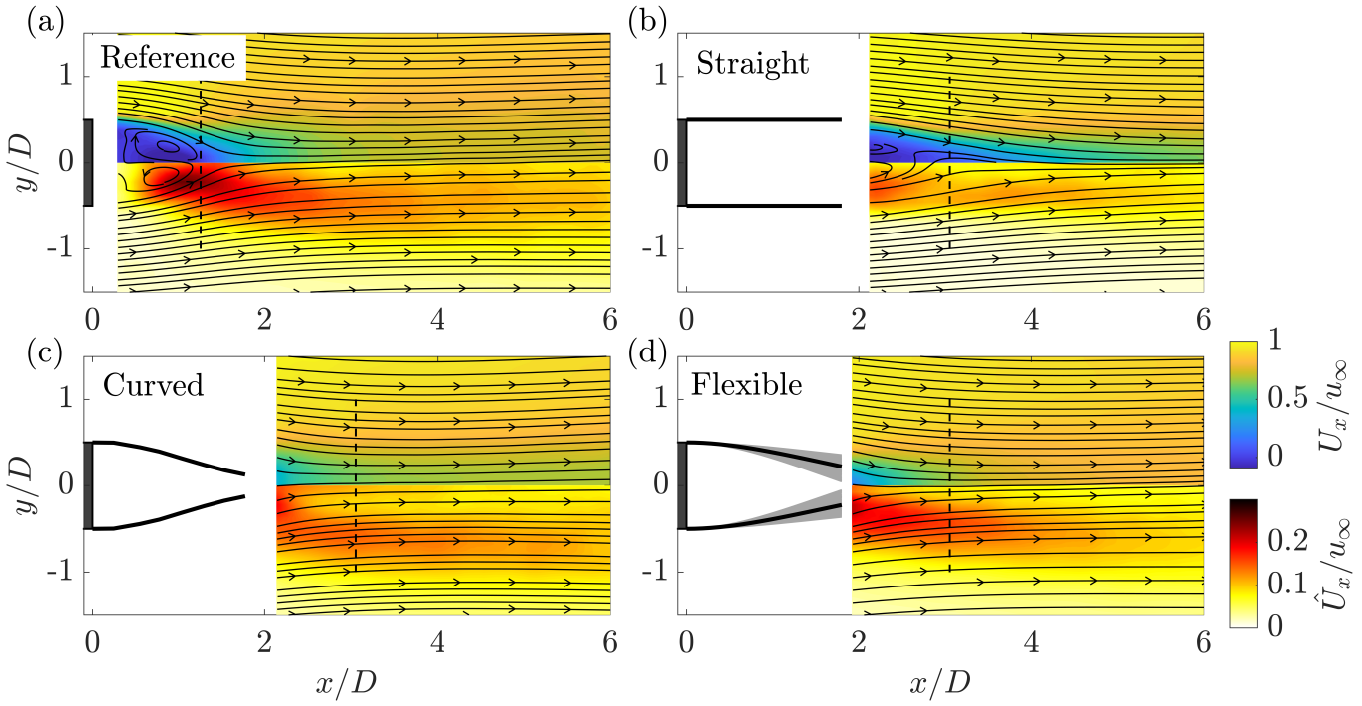

Figure 6. Contours of time-averaged of streamwise velocity, U_x, (top half of each panel) and contours of the time-averaged streamwise velocity fluctuations, $\hat{U}_x$, (bottom half of each panel) corresponding to: (a) Reference case; (b) Straight rigid filaments; (c) Curved rigid filaments and (d) Flexible filaments configurations. The corresponding averaged flow streamlines (U_x, U_y) are also included included. In (d) the filament vibrations are represented by a gray area, while the spatio-temporal averaged filament deflection is shown in black. A black dashed line marks the velocity profile position for Fig. 7. Data corresponding to $Re \simeq 5015$ ($U^* \simeq 2.38$).

two-dimensional wakes. These flow fluctuations are related to the generation of unsteady lift force fluctuations and the consequent increase of drag. In that regard, Fig. 7(b) depicts the classical evolution of streamwise velocity fluctuations at $y = 0$ for the reference case, with a peak that places the vortex formation length [12] of the shed vortices (at $x/D \simeq 1.5$). After that position, the velocity fluctuations decay due to the viscous dissipation and pressure recovery. For the straight configuration, the filaments move away the formed vortices and the associated flow fluctuations are reduced, as it can be seen in Figs. 5, 6. The curved and flexible filaments depict similar trends, illustrating the decay of flow fluctuations observed for the reference case. Interestingly, the streamwise extent of the near wake velocity fluctuations at $y/D = 0$ is considerably reduced with the flexible filaments, reaching a constant value of velocity fluctuations around $x/D \simeq 4$. As previously mentioned in reference to Fig. 6, in both the curved and flexible configurations, the shape of the filaments, adapted to the flow, causes a change in the averaged vectors at separation, inducing more intense transverse velocities. This effect also increases the level of transverse velocity fluctuations since the vortex interaction during vortex shedding is no longer occurring parallel to the axial flow direction but in the center of the wake (see Fig 5c,d). To illustrate that, Fig. 7(c) shows the transverse velocity fluctuations evolution along the flow direction. The curves from flexible and curved filaments maintain approximately the same trend as the reference case across the entire velocity range. However, the straight rigid filaments, reduce significantly the transverse velocity fluctuations, as discussed in Sect. III B.

Regarding the transversal direction, we depict in Fig. 7(d) the streamwise velocity cross-sectional profiles for the 4 tested configurations. The selected streamwise position is $x/D \simeq 1.26$ for the reference case (at the maximum flow fluctuations location) and at $x/D = 3.06$ for the filament cases (Straight, Curved, Flexible) to maintain the distance between the selected positions and the different trailing edges. These positions can be seen in Fig. 6, marked by black dashed lines indicating both the x-position and the transversal distance considered. The transversal profiles, illustrated in Fig. 7(d), obtained at $Re \simeq 5015$ depict a strong velocity gradient at $y/D \pm 0.5$ for the reference and straight cases. These gradients are reduced when curved and flexible filaments are set, also, the negative velocities reached by these configurations is smaller, indicating a different wake formation mechanism and an eventually lower drag coefficient.

Streamwise velocity and turbulent kinetic energy profiles at the mentioned streamwise positions are shown in Figs. 7(e,f). In all cases, the streamwise fluctuations show a predominant double peak in the transverse direction as

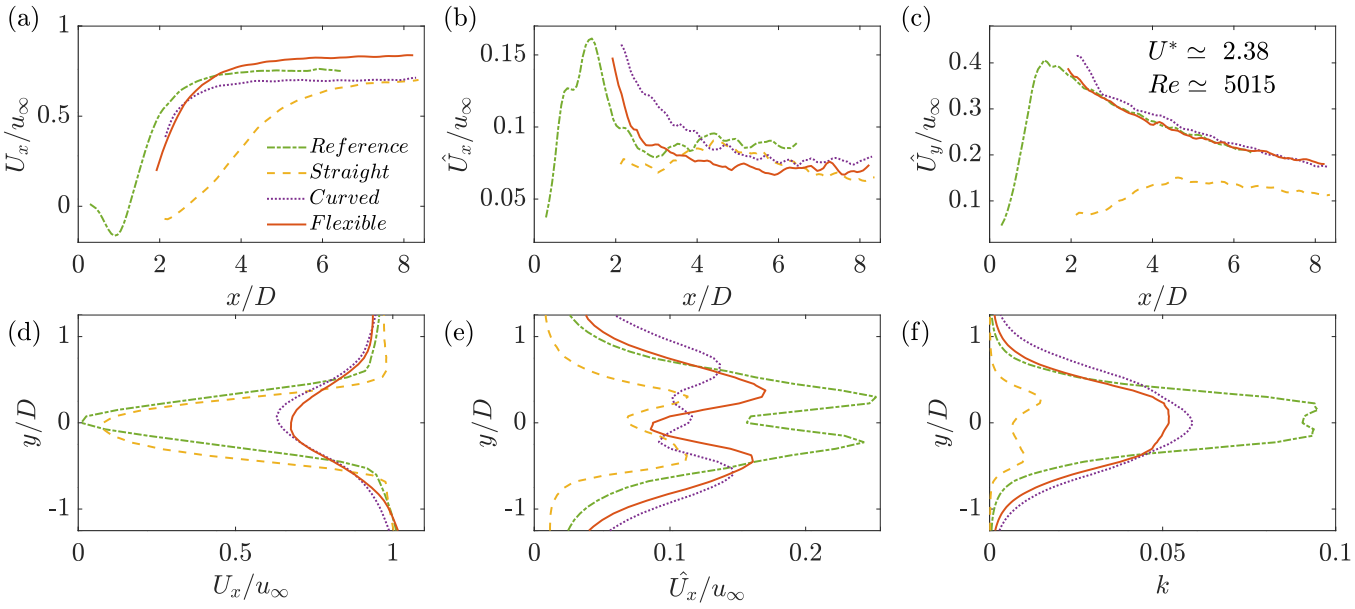

Figure 7. (a) Time-averaged streamwise velocity longitudinal profiles, U_x. (b) Time-averaged streamwise velocity fluctuations longitudinal profiles, $\hat{U}_x$. (c) Time-averaged transversal velocity fluctuations longitudinal profiles, $\hat{U}_y$. (d) Time-averaged streamwise velocity transversal profiles, U_x, (e) Time-averaged streamwise velocity fluctuations transversal profiles, $\hat{U}_x$ and (f) Turbulent kinetic energy transversal profiles k. The longitudinal profiles are selected at $y/D = 0$. The transversal profiles are placed $x/D \simeq 1.26$ for the reference case and at $x/D \simeq 3.06$ for the other configurations (see Fig. 6), at $Re \simeq 5015$ ($U^* \simeq 2.38$). The four configurations represented are: the Reference case (green solid line); Straight rigid filaments (yellow dashed line); Curved rigid filaments (purple dotted line) and Flexible filaments (orange solid line).

evidenced by Figs. 5 and 6, indicating the shedding of alternative vortices detached from each side of the body. The curved case exhibits a third, smaller peak in the central part of the body, which is linked to the vortex interaction taking place in the middle of the wake (see Figs. 5c, 7e). However, the reference case displays the typical transverse distribution of flow fluctuations in the transverse velocity for two-dimensional wakes behind blunt bodies [46], with two symmetrical peaks of streamwise velocity fluctuations at the end of the recirculation region (see Fig. 7e). These flow oscillations, in addition to the transverse flow fluctuations, generate a zone of high turbulent kinetic energy, k, in the center of the wake (see Fig. 7f) and are responsible for generation of large hydrodynamic forces. Notably, the straight case significantly reduces these flow fluctuations due to the delay of flow separation until the extended trailing edges, generating long shear layers that need to be developed to induce any unsteadiness in the flow (see Fig. 5). Furthermore, the curved and flexible filaments modify the flow direction at $x/D = 0$, which in turn alters the flow fluctuations downstream. They exhibit similar transverse distributions of flow fluctuations, with intermediate unsteadiness levels between the reference and straight cases. However, the transversal extension of these flow fluctuations is slightly greater than in the other two configurations. Finally, the flexible filaments generate the largest streamwise velocity fluctuations at $y/D \pm 0.4$, closer to the symmetry axis compared to the other configurations and nearer to the reference case. In this setup, the flow fluctuations are likely driven by the vibrations of the filaments.

D. Velocity deficit and drag estimation

To quantitative characterize the flow changes, we next focus on the velocity deficit in the near wake — the reduction in U_x due to the influence of the body relative to the u_∞, i.e., $U_x/u_\infty < 1$ — from which we can compute an estimation of the drag force, C_D, based on the integration of the momentum equation in the streamwise direction, as in [47, 48]. Thus, we have computed the spatio-temporal averaged streamwise velocity, $\langle U_x/u_\infty \rangle$, distribution along the wake to compare the different configurations in terms of velocity deficit. These velocity distributions are averaged in the range $y/D \pm 1.25$ to cover the transversal extension of the wake for each streamwise location. Thus, Fig. 8 represents the global streamwise velocity deficit in the near wake of the four tested configurations for three selected flow conditions, which are representative of different qualitative responses of the flexible filaments.

As observed in Fig.8(a-c), the recirculation zone is similar between the reference and straight cases, with nearly parallel velocity deficit distributions between both configurations for the three selected flow conditions, the only

difference being an offset corresponding to the $x/D = 1.8$ extension of the straight filaments. The curved configuration produces a smaller velocity deficit than the straight cavity for all the displayed conditions. Interestingly, there is a increasing velocity reduction further downstream from the base that is not seen for the other configurations.

The increasing deformation of the flexible filaments, as U^* grows, has a clear effect on the velocity deficit in the wake behind the body. For low flow velocities, i.e. $U^* \simeq 0.533$, the flow loading is not able to induce deformation on the flexible filaments (see inset in Fig. 8d). As a result, the pre-existing outward deflection alters the velocity in the wake, displaying a trend that differs from other configurations. However, when the filaments reconfiguration takes place, as e.g. for $U^* \simeq 1.57$, the corresponding streamwise velocity distribution starts to resemble those of the other configurations, especially that provided by the curved filaments. That said, the velocity deficit is stronger for the flexible filaments, since the averaged reconfiguration angle is still moderate, $\langle\Theta\rangle \simeq 6^\circ$ (see Fig. 8e). In the saturated phase of response, $U^* > 1.77$, both flexible and curved configurations shows a very similar velocity deficit in the near wake. However, the velocity decrease observed in the far wake for the curved case is not seen in the flexible case, which may indicate an advantageous reduction of the drag coefficient due to passive, dynamic reconfiguration.

The analysis of the spatially averaged streamwise velocity, $\langle U_x/u_\infty\rangle$, in relation to velocity deficit enables us to assess changes in the near wake, associated also with pressure and velocity fluctuation levels, as well as in the far wake, where the average velocity significantly influences the drag on the D-shaped body. From here, we have estimated the drag force, C_D, based on the time-averaged flow data by integrating the momentum equation in the streamwise direction following [47]:

$$C_D(x) = \int_{-1.25D}^{1.25D} \frac{U_x}{u_\infty}(u_\infty - \frac{U_x}{u_\infty})\ dy. \tag{2}$$

Note that such estimation is intimately related to the velocity deficit and does not take into account the contribution of pressure and Reynolds stresses to drag. However, these two factors are mainly relevant in the near wake and, consequently, direct comparisons between configurations based on $C_D(x)$ will be next made in the far wake, where approximate asymptotic velocity distribution are obtained.

The distributions of $C_D(x)$ are displayed in Fig. 8(d-f) for the different configurations and selected flow conditions. As observed therein, the trends of drag estimate for the reference and straight configurations remain nearly parallel over the streamwise direction for the studied velocity range. Initially, for $Re \simeq 1125$, the straight filaments seemingly increase the body's drag in the far wake. However, at higher flow velocities, some drag reduction is observed, as the filaments help to displace the wake region away from the body. As far as the curved filaments is concerned, at low reduced velocity, e.g. $U^* \simeq 0.533$ ($Re \simeq 1125$), a significant drag increase is observed in the far wake, with a steeper trend than that observed for the straight rigid filaments (see Fig. 8d). However, as the velocity increases, this drag increase in the far wake is attenuated and the drag globally decreases in comparison with the reference case, displaying a trend which is similar to that of the straight filaments (see Fig. 8e,f). Finally, the flexible filaments effectively reduce drag across the entire analyzed wake region. Despite their low reconfiguration and oscillation, they significantly reduce drag at low velocities (see Fig. 8d) possibly due to the wake stabilization. As U^* increases, the flexible filaments configuration consistently proves to be the most effective at reducing drag, highlighting the efficiency of these devices with a certain level of flexibility.

We will next examine how the Reynolds number (Re) and characterized velocity (U^*) affect the wake changes caused by different devices. For this comparison, we have chosen a streamwise position of $x/D \approx 3.06$ ($x/D \approx 1.26$ for the reference case) to analyze the averaged streamwise velocity and turbulent kinetic energy in the near wake. Additionally, we selected a position of $x/D \approx 5$ ($x/D \approx 3.2$ for the reference case) to assess the drag coefficient, as it is best estimated in the far wake. This allows us to evaluate both the averaged and fluctuating velocities in the near wake, as well as the estimated drag in the far wake, providing a comprehensive understanding of how configurations affect different flow conditions.

Figure 9 depicts the spatio-temporal, averaged streamwise velocity distribution (both averaged, $\langle U_x/u_\infty\rangle$, and fluctuating, $\langle k\rangle$, components) and the estimated drag, C_D, for the aforementioned relative locations. Note that, by keeping the same relative position to the trailing edges of the filaments, the comparison of the tested devices can be considered consistent. The reference case depicts a slight decrease (respectively, increase) of the velocity deficit (respectively, estimated drag) for the studied range of Re numbers (see Fig. 9a, b), suggesting the development of a more intense wake. The straight filaments show a similar trend (only small differences are observable at low flow velocities) and induce drag reduction, in comparison with the reference case, for $Re > 2000$. Besides, the curved filaments display an important reduction of the velocity deficit and the drag, which is however reverted as Re grows above $Re > 4000$. The trends are qualitatively different for the configuration with flexible filaments. For low reduced velocities, $U^* < 1$, the velocity deficit is similar to that one corresponding to rigid filaments, as the flow loading cannot still deform the flexible filaments. Interestingly, the estimated drag from the far wake is small, probably due to the wake steadiness observed under these conditions (also supported by Fig. 9c). Then, a sudden velocity deficit decrease and drag increase is observed at $U^* \simeq 1$. This drag enhancement might be related to the abrupt increase of

filaments fluctuations which is not yet overcome by the mild adaption of the averaged shape. The situation is however soon reverted, as the filaments adopt a quasi-static reconfiguration at larger U^*. In fact, for the saturation regime, $U^* > 1.77$, the curved and flexible flaps display similar velocity deficit and estimated drag. Notwithstanding, the drag increase observed when $Re > 4000$ for the curved case is not seen for the flexible filaments, which are shown to efficiently improve the aerodynamic coefficient.

We will finally focus on the analysis of the flow fluctuations, estimated here with the spatio-temporal average of the turbulent kinetic energy over $y/D \pm 1.25$, $\langle k \rangle$, which are displayed in fig. 9(c) for the four configurations. This analysis complements the conclusions extracted for the velocity deficit $\langle U_x/u_\infty \rangle$ and the estimated drag C_D as the wake fluctuations are known to contribute to the drag generation. For the reference case, the flow unsteadiness seems to converge around $Re \simeq 1755$, as it happened with the shedding frequency (see Fig. 4c). As previously observed, straight filaments significantly reduce wake unsteadiness across all tested Re, maintaining a constant fluctuation amplitude throughout the entire range. Moreover, curved filaments provoke a wider near wake (as seen in Fig. 8c) which produces larger spatio-temporal flow fluctuations in comparison with other configurations. The distinct behavior of the flexible filaments is also evident in Fig. 9(b). At low reduced velocities, flow fluctuations are minimal, as the flow is insufficient to displace the filaments or generate a significant near wake. As the flow velocity increases, fluctuations sharply rise, coinciding with the increasing passive reconfiguration and vibration of the filaments. However, at highest reduced velocities, $U^* > 1.77$, the flexible filaments behave similarly to the curved configuration, with minimal impact from filament vibrations on wake unsteadiness.

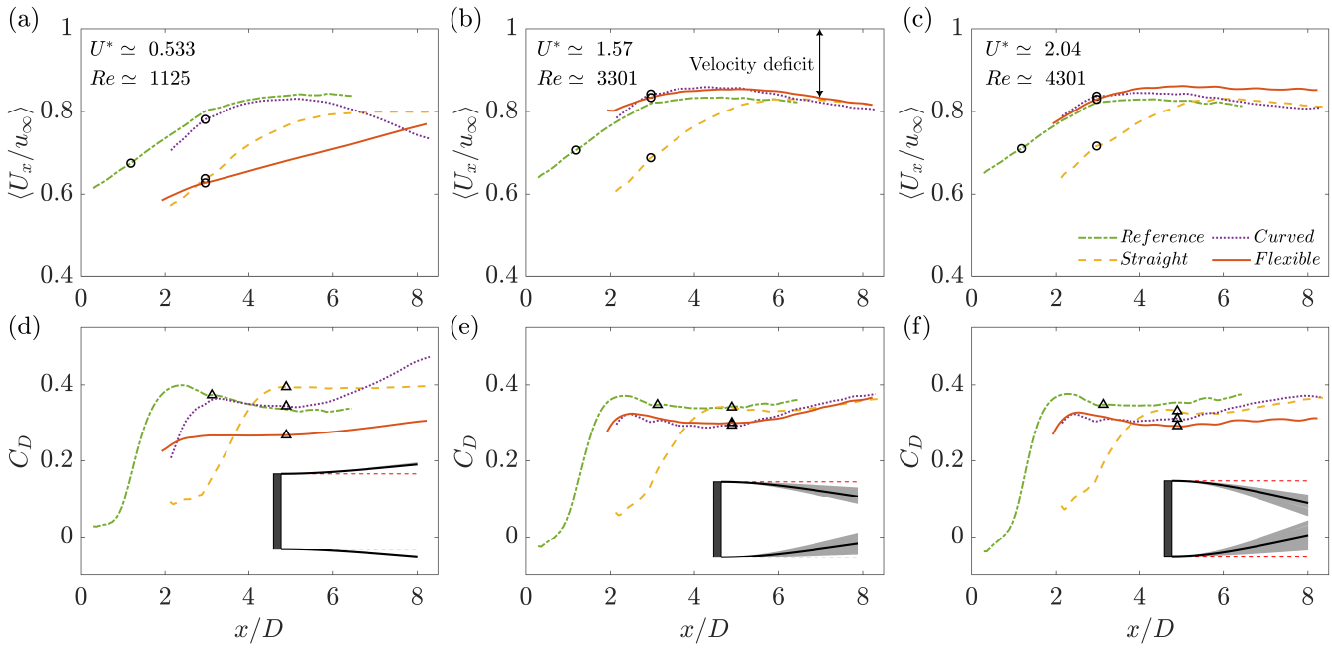

Figure 8. Spatio-temporal averaged streamwise velocity, $\langle U_x/u_\infty \rangle$ (a,b,c) and estimated drag, C_D, (d,e,f), streamwise evolution at: (a,d) $Re \simeq 1125$ ($U^* \simeq 0.533$), (b,e) $Re \simeq 3301$ ($U^* \simeq 1.57$) and (c,f) $Re \simeq 4301$ ($U^* \simeq 2.04$) for the four tested configurations. The Reference case is represented in green solid dashed-dotted lines; Straight rigid filaments is illustrated by yellow dashed lines; Curved rigid filaments in purple dotted lines and Flexible filaments are depicted in orange solid lines. In each case and configuration at subfigure a, b and c, the location chosen for the study of the velocity profiles and the Re dependence is indicated by a black circle ($\langle U_x/u_\infty \rangle$) or a black triangle ($C_D$). For each case, the spatio-temporal averaged deflection of the flexible filaments is shown in an inset by black solid lines, the filament vibrations are depicted with a gray shading, and the reference position of the filaments are indicated by red dashed lines.

IV. CONCLUSIONS

In this study, we experimentally compared the effect of 4 different afterbody configurations in the flow around a two-dimensional D-shaped blunt body. The main goal of the work was to asses the efficiency of rear flexible filaments to reduce the wake extent and the flow unsteadiness behind the body, which contribute to the generation of undesirable forces in several applications. This problem is a simplified configuration of many associated industrial and environmental problems, and the study may constitute a first approximation to a quasi two-dimendional analysis (note

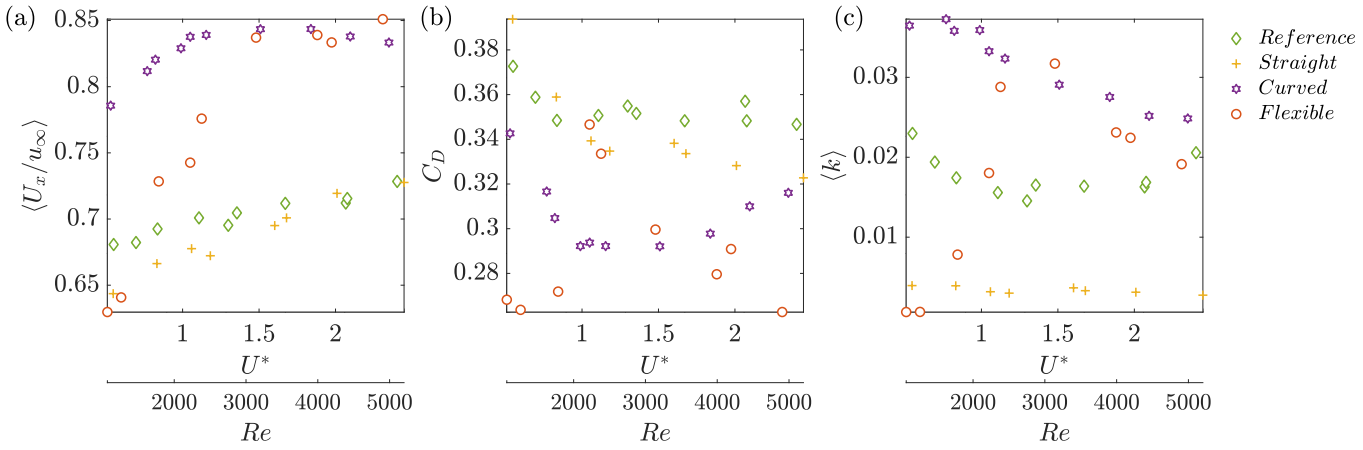

Figure 9. Evolution of the (a) spatio-temporal averaged streamwise velocity, $\langle U_x/u_\infty \rangle$, (b) estimated drag, C_D, and (c) spatio-temporal averaged turbulent kinetic energy, $\langle k \rangle$, with Re (U^*). The four configurations represented are: the Reference case (green diamonds); Straight rigid filaments (yellow crosses); Curved rigid filaments (purple stars) and Flexible filaments (orange circles). Note that the spatial averaging in (a) and (c) has been performed over $y/D \pm 1.25$ at $x/D \simeq 1.26$ for the reference case and at $y/D \pm 1.25$ and $x/D \simeq 3.06$ for the other configurations. For the drag analysis, the reference point is set at $x/D \simeq 3.2$ for the reference case and $x/D \simeq 5$ for the others.

that a value of the aspect ratio H/D larger than the one used here might be required to characterize more canonical two-dimensional responses). The experiments, performed in a closed-loop water channel, were conducted at different flow velocities to analyze the relation between the tested afterbodies and the corresponding near wake. In the case of the flexible filaments, they are seen to interact with the flow around the body in different regimes (see Fig. 3). At small flow velocities, $U^* < 1$, the filaments are not affected by the flow and they preserve their initial loading. When the flow velocity is increased $1 < U^* < 1.77$, the flexible filaments start to passively reconfigure as well as displaying mild vibrations (see Fig. 3). The response of the flaps saturates at $U^* > 1.77$, fixing an averaged tip deflection deformation of $\langle \Theta \rangle \simeq 9°$ associated to $\langle \hat{\Theta} \rangle \simeq 4°$ vibrations. This saturated passive reconfiguration is selected to produce the curved filament configuration. The response of the filaments is almost two-dimensional (see Fig. 2) and it is coupled with the vortex shedding produced in the wake behind the model (see Fig. 4). This coupling induces the reduction of the shedding frequency when this flexible filaments are implemented. Regarding the wake changes induced by the different afterbodies, in comparison with the reference case, flexible and rigid (straight or curved) filaments delay the flow separation, increasing the distance between the recirculating flow or velocity fluctuations and the body base, eventually increasing the base pressure and reducing the unsteady loads on the body (see Figs. 5, 6, 7). Quantitatively speaking, the streamwise velocity deficit in the wake and the corresponding estimated drag are reduced when the filaments are employed (see Figs. 8 and 9), especially for $U^* > 1$, when the flexible filaments interact with the flow. In addition, their vibrating dynamics affects the wake features, improving the aerodynamic features of the body in comparison to the rigid curved ones. These results prove the potential of flexible filaments as efficient solution for aerodynamic improvement through passive reconfiguration, without the disadvantages that may feature continuous flexible parts (such as significant loads and potential torsional deformations). That said, its application to engineering problems may require a deeper analysis under more complex geometries and flow conditions.

ACKNOWLEDGMENTS

The authors would like to thank Alejandro Ibarra, Jean-François Egea, Amaury Fourgeaud, Xavier Benoit-Gonin, Olivier Brouard, Laurent Quartier and Jose Eduardo Wesfreid for their support in the preparation of the experiments and the establishment of this international scientific collaboration. The authors gratefully acknowledge the funding provided by the projects TED2021-131805B-C21, TED2021-131805B-C22 and PID2022-140433NA-I00 financed by the Spanish MCIN/ AEI/10.13039/501100011033/, the European Union NextGenerationEU/PRTR and FEDER, UE respectively. J.C.M.H. also acknowledges for the support of the Spanish MECD through FPU20/07261 and EST23/00743.

REFERENCES

[1] H. Choi, W.-P. Jeon, and J. Kim, Control of flow over a bluff body, Annu. Rev. Fluid Mech. **40**, 113 (2008).
[2] C. H. K. Williamson and R. Govardhan, Vortex-induced vibrations, Annu. Rev. Fluid Mech. **36**, 413 (2004).
[3] T. Sarpkaya, A critical review of the intrinsic nature of vortex-induced vibrations, J. Fluids Struct. **19**, 389 (2004).
[4] M. P. Païdoussis, S. J. Price, and E. De Langre, *Fluid-structure interactions: cross-flow-induced instabilities* (Cambridge University Press, 2010).
[5] J.-C. Lecordier, L. Hamma, and P. Paranthoen, The control of vortex shedding behind heated circular cylinders at low Reynolds numbers, Exp. Fluids **10**, 224 (1991).
[6] N. Tombazis and P. W. Bearman, A study of three-dimensional aspects of vortex shedding from a bluff body with a mild geometric disturbance, J. Fluid Mech. **330**, 85 (1997).
[7] H. Park, D. Lee, W.-P. Jeon, S. Hahn, J. Kim, J. Kim, J. Choi, and H. Choi, Drag reduction in flow over a two-dimensional bluff body with a blunt trailing edge using a new passive device, J. Fluid Mech. **563**, 389 (2006).
[8] M. Pastoor, L. Henning, B. R. Noack, R. King, and G. Tadmor, Feedback shear layer control for bluff body drag reduction, J. Fluid Mech. **608**, 161 (2008).
[9] D. J. Parkin, M. C. Thompson, and J. Sheridan, Numerical analysis of bluff body wakes under periodic open-loop control, J. Fluid Mech. **739**, 94 (2014).
[10] R. Li, J. Borée, B. R. Noack, L. Cordier, and F. Harambat, Drag reduction mechanisms of a car model at moderate yaw by bi-frequency forcing, Phys. Rev. Fluids **4**, 034604 (2019).
[11] S. Boury, B. Thiria, R. Godoy-Diana, G. Artana, J. E. Wesfreid, and J. d'Adamo, Forced wakes far from threshold: Stuart-Landau equation applied to experimental data, Phys. Rev. Fluids **3**, 091901 (2018).
[12] P. W. Bearman, The effect of base bleed on the flow behind a two-dimensional model with a blunt trailing edge, Aeronaut. Quart. **18**, 207 (1967).
[13] A. Sevilla and C. Martínez-Bazán, Vortex shedding in high Reynolds number axisymmetric bluff-body wakes: local linear instability and global bleed control, Phys. Fluids **16**, 3460 (2004).
[14] L. Henning, M. Pastoor, R. King, B. R. Noack, and G. Tadmor, Feedback control applied to the bluff body wake, in *Active Flow Control: Papers contributed to the Conference "Active Flow Control 2006", Berlin, Germany, September 27 to 29, 2006* (Springer, 2007) pp. 369–390.
[15] R. D. Brackston, J. M. García de la Cruz, A. Wynn, G. Rigas, and J. F. Morrison, Stochastic modelling and feedback control of bistability in a turbulent bluff body wake, J. Fluid Mech. **802**, 726–749 (2016).
[16] W. A. Mair, The effect of a rear-mounted disc on the drag of a blunt-based body of revolution, Aeronaut. Quart. **16**, 350 (1965).
[17] E. Sanmiguel-Rojas, J. I. Jiménez-González, P. Bohorquez, G. Pawlak, and C. Martínez-Bazán, Effect of base cavities on the stability of the wake behind slender blunt-based axisymmetric bodies, Phys. Fluids **23** (2011).
[18] J. Cai and T. L. Chng, On vortex shedding from bluff bodies with base cavities, Phys. Fluids **21** (2009).
[19] R. W. Kruiswyk and J. C. Dutton, Effects of a base cavity on subsonic near-wake flow, AIAA Journal **28**, 1885 (1990).
[20] W. A. Mair, Drag-reducing techniques for axi-symmetric bluff bodies, in *Aerodynamic drag mechanisms of bluff bodies and road vehicles* (Springer, 1978) pp. 161–187.
[21] T. Han, D. C. Hammond Jr, and C. J. Sagi, Optimization of bluff body for minimum drag in ground proximity, AIAA Journal **30**, 882 (1992).
[22] H. Choi, J. Lee, and H. Park, Aerodynamics of Heavy Vehicles, Annu. Rev. Fluid Mech. **46 (1)**, 441 (2014).
[23] A. Martín-Alcántara, E. Sanmiguel-Rojas, C. Gutiérrez-Montes, and C. Martínez-Bazán, Drag reduction induced by the addition of a multi-cavity at the base of a bluff body, J. Fluid. Struct. **48**, 347 (2014).
[24] M. Lorite-Díez, J. I. Jiménez-González, C. Gutiérrez-Montes, and C. Martínez-Bazán, Drag reduction of slender blunt-based bodies using optimized rear cavities, J. Fluids Struct. **74**, 158–177 (2017).
[25] M. Lorite-Díez, J. I. Jiménez-González, C. Gutiérrez-Montes, and C. Martínez-Bazán, Effects of rear cavities on the wake behind an accelerating D-shaped bluff body, Phys. Fluids **30** (2018).
[26] M. Lorite-Díez, J. I. Jiménez-González, L. Pastur, C. Martínez-Bazán, and O. Cadot, Experimental sensitivity analyses of modes to blowing at the base of a 3D bluff body, J. Fluid Mech. **883**, A53 (2020).
[27] S. Alben, M. Shelley, and J. Zhang, Drag reduction through self-similar bending of a flexible body, Nature **420**, 479 (2002).
[28] C. García-Baena, J. I. Jiménez-González, C. Gutiérrez-Montes, and C. Martínez-Bazán, Numerical analysis of the flow-induced vibrations in the laminar wake behind a blunt body with rear flexible cavities, J. Fluid. Struct. **100**, 103194 (2021).
[29] C. García-Baena, J. M. Camacho-Sánchez, M. Lorite-Díez, C. Gutiérrez-Montes, and J. I. Jiménez-González, Drag reduction on a blunt body by self-adaption of rear flexibly hinged flaps, J. Fluid. Struct. **118**, 103854 (2023).
[30] D. L. Harder, O. Speck, C. L. Hurd, and T. Speck, Reconfiguration as a prerequisite for survival in highly unstable flow-dominated habitats, J. Plant Growth Regul. **23**, 98 (2004).
[31] X. Zhang and H. Nepf, Flow-induced reconfiguration of aquatic plants, including the impact of leaf sheltering, Limnol. Oceanogr. **65**, 2697 (2020).

[32] S. Vogel, Drag and reconfiguration of broad leaves in high winds, J. Exp. Bot. **40**, 941 (1989).
[33] E. de Langre, Effects of wind on plants, Annual Review of Fluid Mechanics **40**, 141 (2008).
[34] R. Abdi, N. Rezazadeh, and M. Abdi, Investigation of passive oscillations of flexible splitter plates attached to a circular cylinder, J. Fluid. Struct. **84**, 302 (2019).
[35] L. Keirsbulck, O. Cadot, J. Basley, and M. Lippert, Base suction, entrainment flux, and wake modes in the vortex formation region at the rear of a three-dimensional blunt bluff body, Phys. Rev. E **108**, 015101 (2023).
[36] M. Chrust, S. Goujon-Durand, and J. E. Wesfreid, Loss of a fixed plane of symmetry in the wake of a sphere, J. Fluid. Struct. **41**, 51 (2013).
[37] L. Klotz, S. Goujon-Durand, J. Rokicki, and J. E. Wesfreid, Experimental investigation of flow behind a cube for moderate Reynolds numbers, J. Fluid Mech. **750**, 73 (2014).
[38] M. Skarysz, J. Rokicki, S. Goujon-Durand, and J. E. Wesfreid, Experimental investigation of the wake behind a rotating sphere, Phys. Rev. Fluids **3**, 013905 (2018).
[39] C. Marais, R. Godoy-Diana, D. Barkley, and J. E. Wesfreid, Convective instability in inhomogeneous media: Impulse response in the subcritical cylinder wake, Phys. Fluids **23** (2011).
[40] B. Wieneke, PIV uncertainty quantification from correlation statistics, Meas. Sci. Technol. **26**, 074002 (2015).
[41] T. L. Hedrick, Software techniques for two-and three-dimensional kinematic measurements of biological and biomimetic systems, Bioinspiration Biomim. **3**, 034001 (2008).
[42] C. García-Baena, J. I. Jiménez-González, and C. Martínez-Bazán, Drag reduction of a blunt body through reconfiguration of rear flexible plates, Phys. Fluids **33(4)**, 045102 (2021).
[43] E. Achenbach and E. Heinecke, On vortex shedding from smooth and rough cylinders in the range of Reynolds numbers 6×10^3 to 5×10^6, J. Fluid Mech. **109**, 239 (1981).
[44] A. Mariotti, G. Buresti, G. Gaggini, and M. V. Salvetti, Separation control and drag reduction for boat-tailed axisymmetric bodies through contoured transverse grooves, J. Fluid Mech. **832**, 514 (2017).
[45] A. Mariotti, G. Buresti, and M. V. Salvetti, Separation delay through contoured transverse grooves on a 2D boat-tailed bluff body: Effects on drag reduction and wake flow features, Eur. J. Mech. B Fluids **74**, 351 (2019).
[46] J. E. Wesfreid, S. Goujon-Durand, and B. J. A. Zielinska, Global mode behavior of the streamwise velocity in wakes, Journal de Physique II **6**, 1343 (1996).
[47] J. M. Anderson, K. Streitlien, D. S. Barrett, and M. S. Triantafyllou, Oscillating foils of high propulsive efficiency, J. Fluid Mech. **360**, 41–72 (1998).
[48] R. Godoy-Diana, J.-L. Aider, and J. E. Wesfreid, Transitions in the wake of a flapping foil, Phys. Rev. E **77**, 016308 (2008).